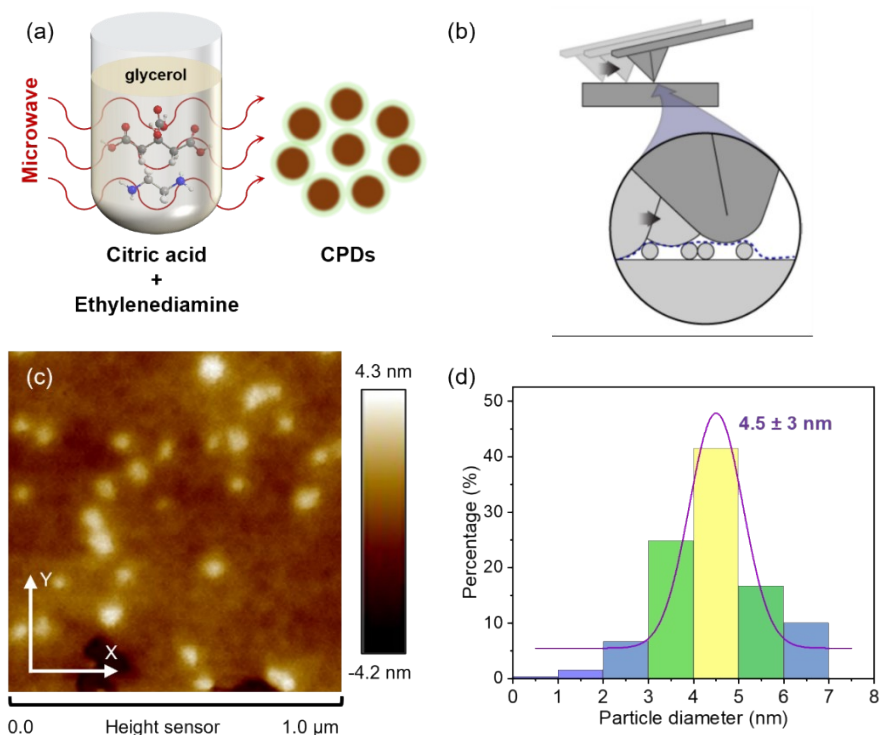


## Supplementary Information

### **Modulating the in-Plane Local Charge Density of Graphene via Carbon Quantum Dots for Enhanced Triiodide Reduction**

Yiwang Ding, Chang Yu,\* Jiangwei Chang, Xuedan Song, Jinhe Yu, Siyi Hou, Yuanyang Xie,  
Jieshan Qiu\*



**Fig. S1.** (a) Schematic illustration of the preparation process for CPDs. (b) The diagrammatic sketch explaining that the probe size causes the error in the X/Y resolution of the AFM image. (c) AFM image of CPDs. (d) The size distribution of the CPDs and the Gauss fit curve is coloured purple.

The measurement results on the X/Y dimension are determined by the scanning path of the probe, which starts from one side of the probe approaching the sample and ends at the other side far away from the sample. But the height sensor is the lifting height of the probe, independent of its size. Therefore, it is more accurate for particles to count the size according to the detected height from the AFM results. **Fig. S1d** is the result that the software of NanoScope Analysis calculates the particle size by analyzing the height threshold of pixel collection.

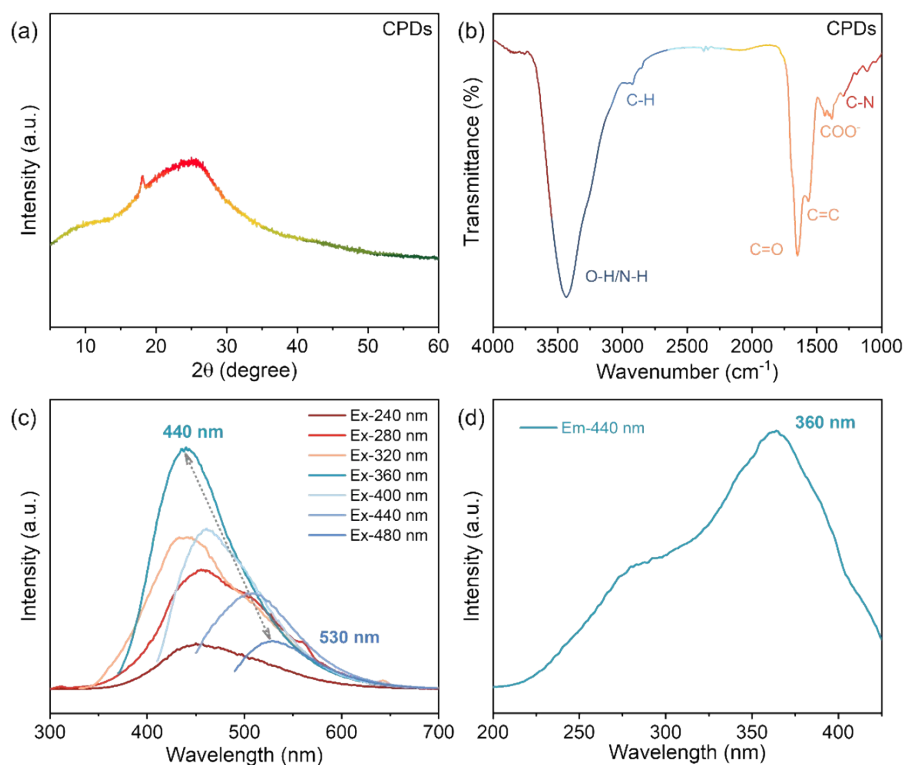


**Fig. S2.** (a) XRD pattern, (b) FT-IR spectrum, (c) photoluminescence (PL) emission spectra at different excitation wavelengths and (d) PL excitation spectrum of CPDs.

In the XRD pattern, as displayed in **Fig. S2a**, the broad peak of CPDs is located at  $25^\circ$  and distinguished from the diffraction peak of graphitic carbon, suggesting that the generated CPDs are assigned to a polymer-carbon hybrid structure. The partial polycondensation reaction makes abundant functional groups and cross-linking oligomer chains pad the crystal structure of CPDs, which results in distortion of the lattice space and the increase of interlayer spacing confirmed in the literature.<sup>1-3</sup> FT-IR was performed for further investigating the functional groups and chemical composition of CPDs (**Fig. S2b**). The absorption bands at about 3433, 2924, 1651, 1564, 1386, and

1294  $\text{cm}^{-1}$  are assigned to O-H/N-H, C-H, C=O, C=C,  $\text{-COO}^-$  and C-N stretching, respectively, further proving the existence of abundant oxygen-containing and nitrogen-containing functional groups.

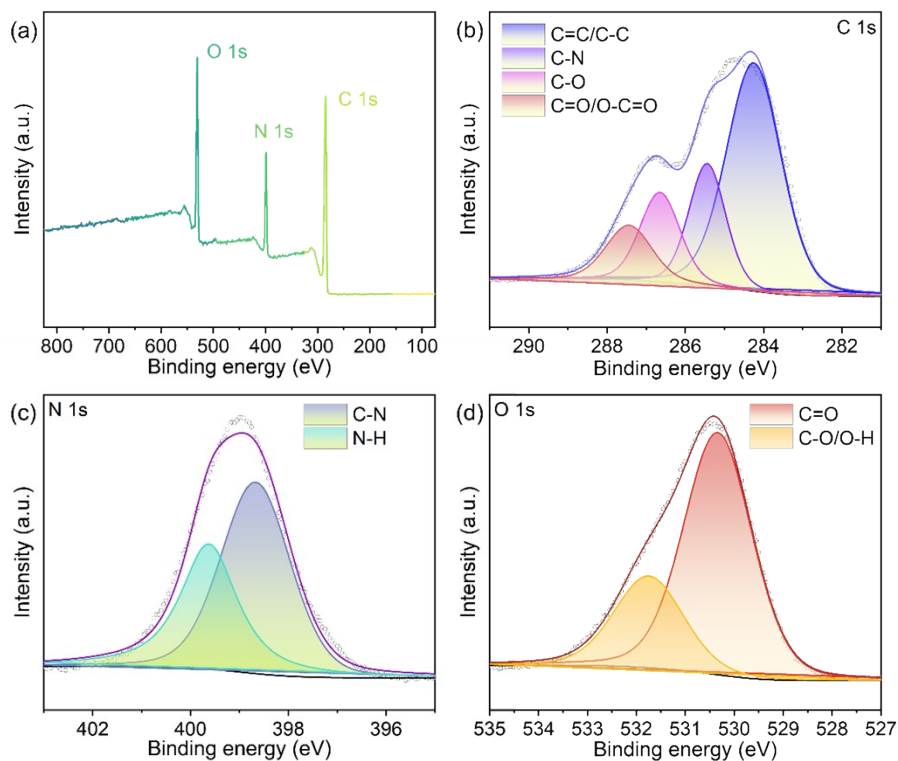


**Fig. S3.** (a) XPS survey spectrum of CPDs. High-resolution XPS spectra of (b) C 1s, (c) N 1s, and (d) O 1s of CPDs.

The surface chemistry of CPDs was explored by XPS, as shown in **Fig. S3**. The survey spectrum (**Fig. S3a**) indicates that as-prepared CPDs contain C, N, and O. High-resolution C 1s spectrum (**Fig. S3b**) of CPDs exhibits detailed peaks at about 284.6, 285.4, 286.6, and 287.6 eV corresponding to C=C/C-C, C-N, C-O, and C=O/O-C=O, respectively,<sup>4, 5</sup> while the N 1s spectrum (**Fig. S3c**) of CPDs can be fitted into two peaks, attributed to C-N (at 398.5 eV) and N-H (at 399.80 eV), respectively.<sup>6</sup> Generation of the C=C bond is ascribed to the aromatization of the particles, and the partial polycondensation reaction retains abundant oxygen-containing and nitrogen-containing functional groups from the

raw materials of ethylenediamine and citric acid.<sup>7</sup> The above results reveal that CPDs are composed of the dehydrated and pre-carbonized core and the unreacted functional groups.

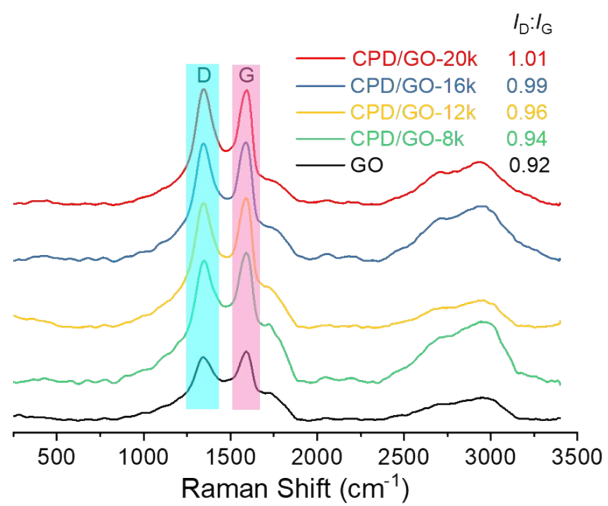


**Fig. S4.** Raman spectra of the CPDs/GO-x and the GO samples.

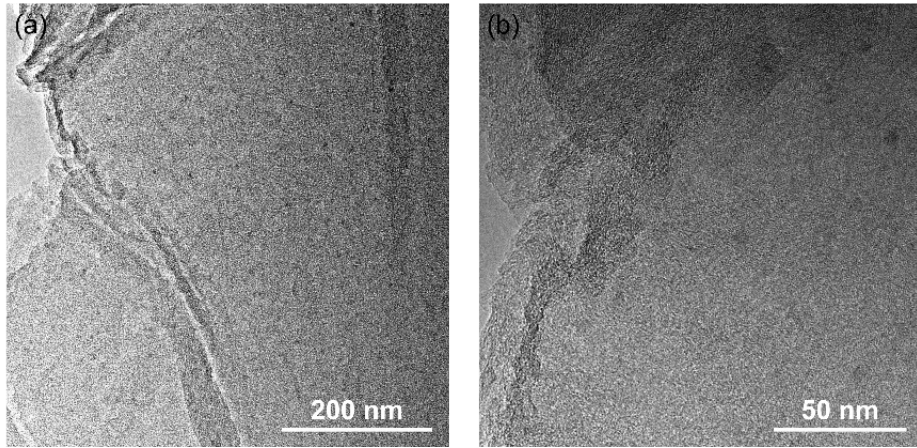


**Fig. S5.** TEM images of CQDs/rGO-16k.

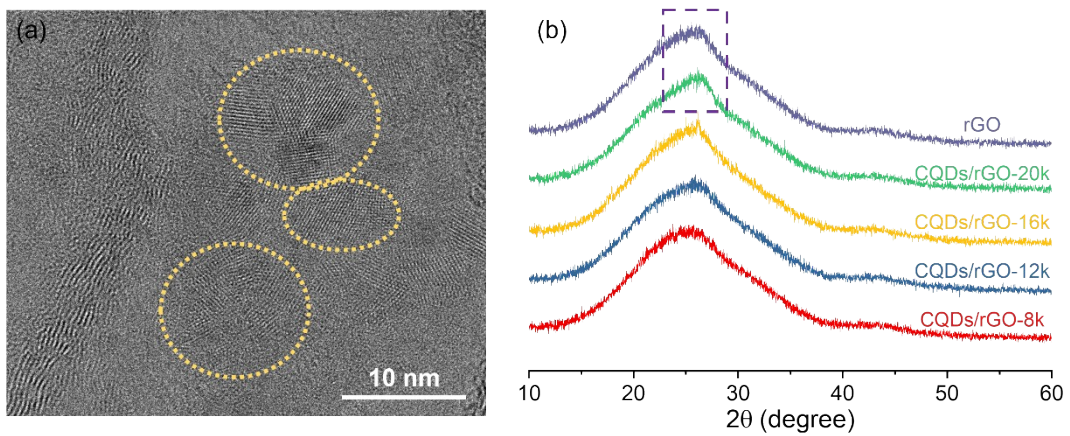


**Fig. S6.** (a) TEM image of CQDs/rGO-20k, where the yellow ellipse area presents slight accumulation. (b) XRD patterns of rGO and CQDs/rGO-x samples.

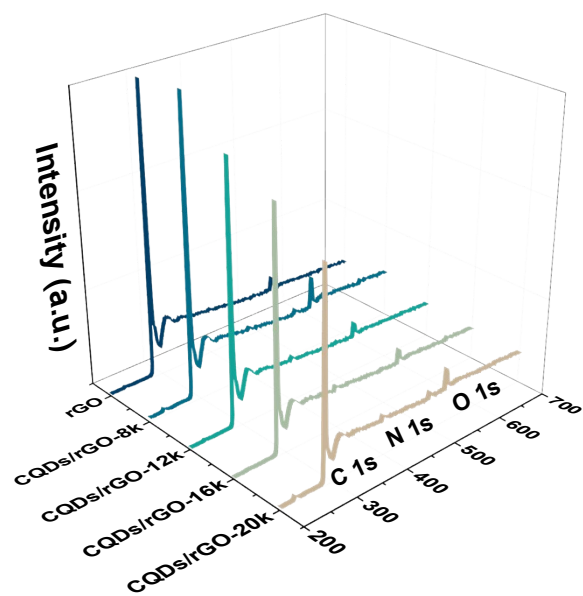


**Fig. S7.** XPS survey spectra of the rGO and various CQDs/rGO-x samples.

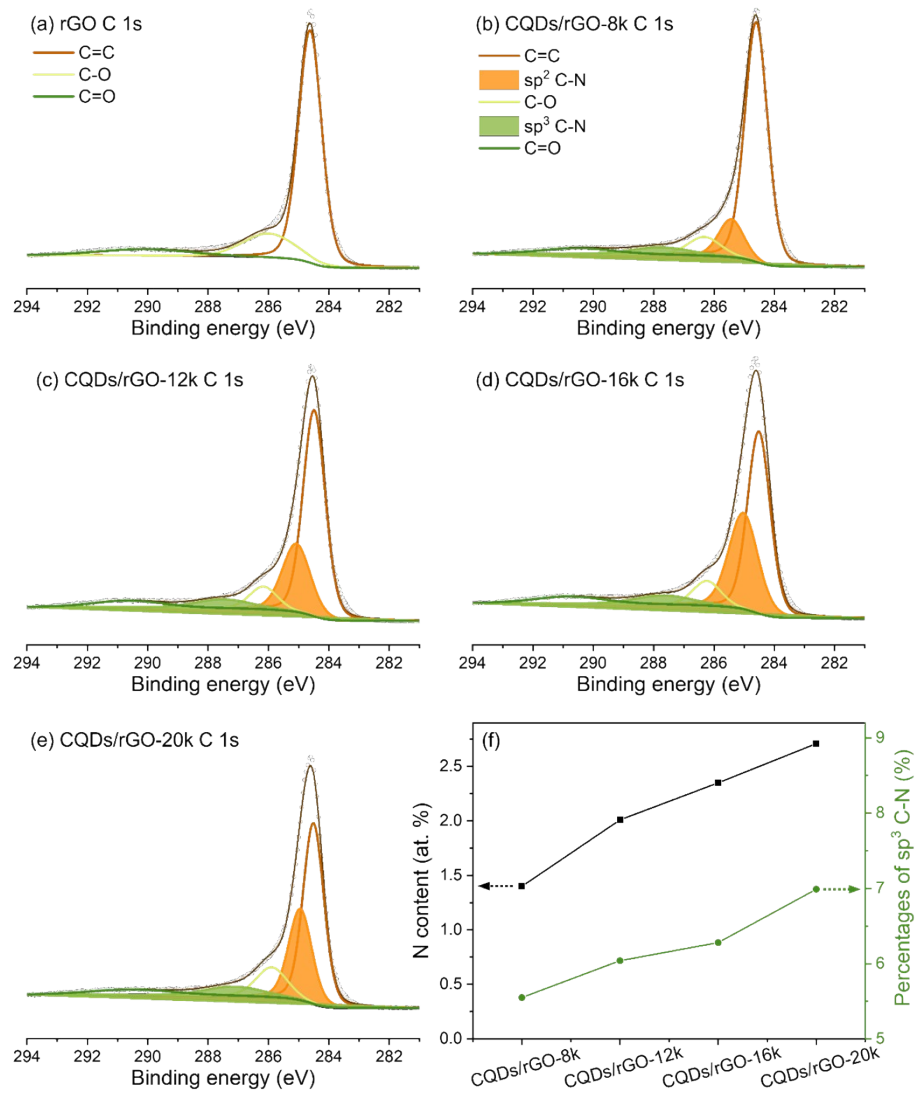


**Fig. S8.** XPS spectra for the C 1s of (a) rGO, (b) CQDs/rGO-8k, (c) CQDs/rGO-12k, (d) CQDs/rGO-16k and (e) CQDs/rGO-20k. (f) The atomic percentage of nitrogen and percentage of sp<sup>3</sup> C-N in the CQDs/rGO-x samples calculated by the area ratios of the peaks in XPS spectra.

The content (at. %) of nitrogen extracted from XPS spectra increased gradually, which further proved the increase of CQDs loading and realizable regulation from CQDs/rGO-

8k to CQDs/rGO-20k. The C 1s spectrum of rGO can be fitted into three peaks at 284.6, 285.6, 290.0 eV (**Fig. S8a**). After rGO coupling with CQDs, C 1s spectra of CQDs/rGO-x samples exhibit the small new peaks at 285.4 and 287.6 eV obtained by peak fitting, suggesting the bonding formation for doped nitrogen atoms bonding with  $sp^2$ -C and  $sp^3$ -C atoms, respectively (**Fig. S8b-e**).<sup>8</sup> Interesting is the finding that  $sp^2$  C-N is ascribed to the lattice doping of N atoms in dense carbon nuclei of CQDs, while the  $sp^3$  C-N bond with the out-of-plane orientation can be considered as the bridging bonds between CQDs and rGO, of which the composite model is confirmed in the literature.<sup>9, 10</sup> Furthermore, the percentages of  $sp^3$  C-N species with gradual growth are also observed as the increase of CQDs loading.

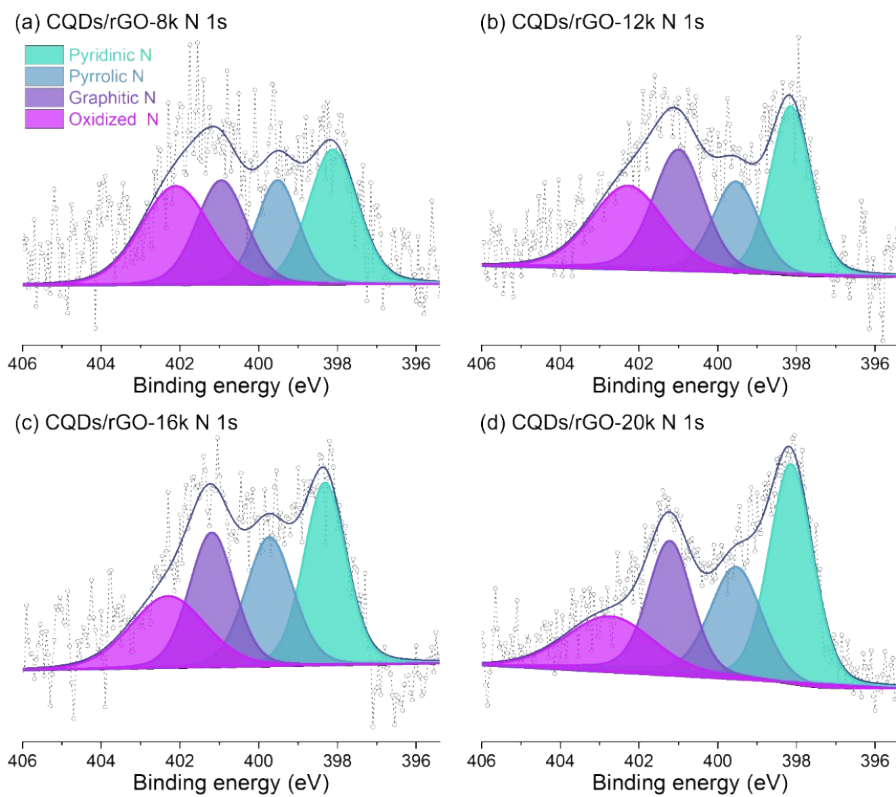


**Fig. S9.** XPS spectra for the N 1s of (a) CQDs/rGO-8k, (b) CQDs/rGO-12k, (c) CQDs/rGO-16k and (d) CQDs/rGO-20k.

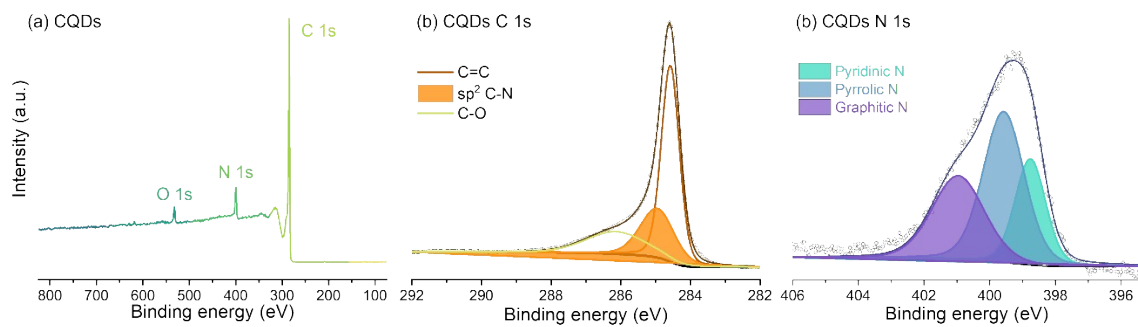


**Fig. S10.** (a) XPS survey spectrum of CQDs. High-resolution XPS spectra of (b) C 1s and (c) N 1s of CQDs.

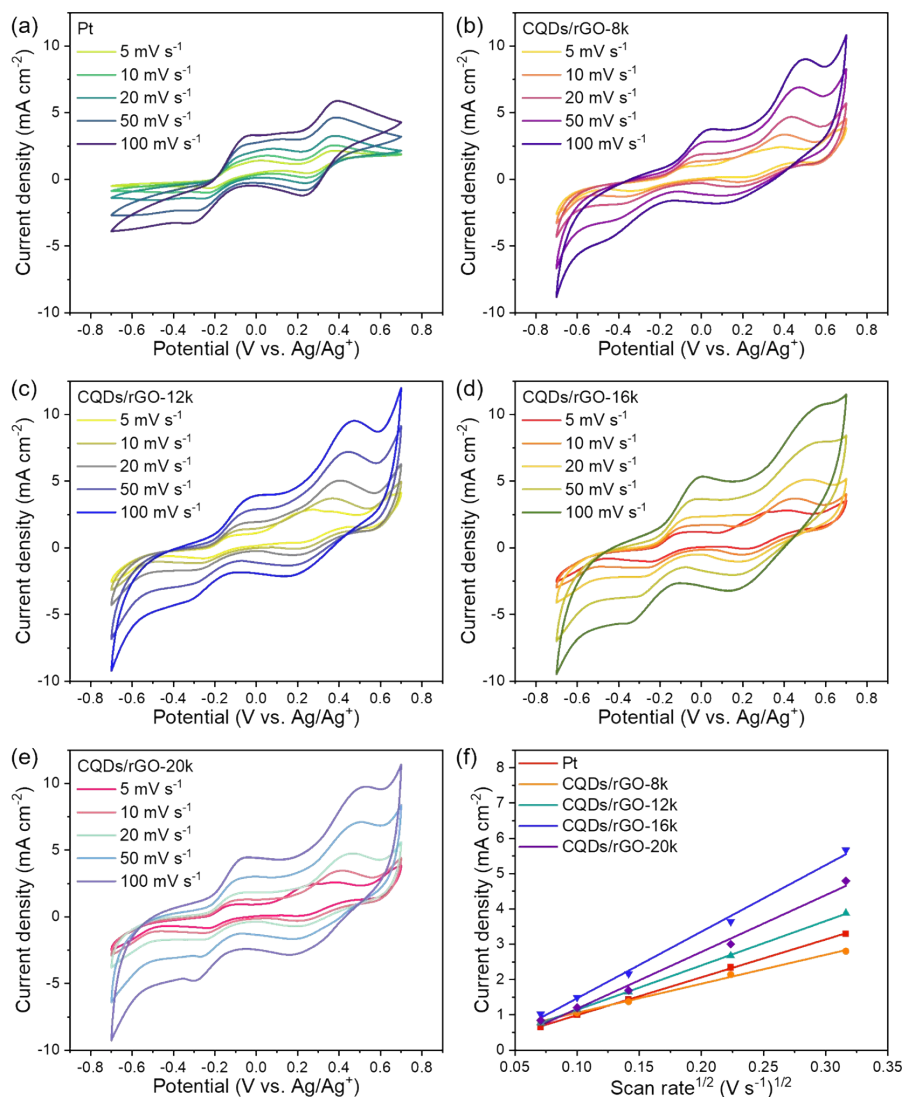


**Fig. S11.** CV curves of (a) Pt and (b-e) CQDs/rGO-x at different scan rates from 5 mV s<sup>-1</sup> to 100 mV s<sup>-1</sup>. (f) The current densities of  $A_{\text{red}}$  occurring at the Pt and CQDs/rGO-x cathodes vs. square root of scan rates.

The CV curves of the 0.5NCNF750-2 and Pt CEs at several scan rates were examined, and there is the relationship of the  $J_{A_{\text{red}}}$  vs. square root of scan rates, which could be explained by Randles-Sevcik theory:  $I_{\text{peak}} = Kn^{3/2}ACD^{1/2}V^{1/2}$ .  $I_{\text{peak}}$  is the peak current, K is

the constant of  $2.69 \times 10^5$ ,  $n$  is the electron transfer number,  $A$  is the electrode area,  $D'$  is the diffusion coefficient of the electrolyte,  $V$  is the scan rate, and  $C$  is the electrolyte concentration.<sup>11</sup> The linear relationship between the  $J_{Ared}$  and the square root of scan rate was demonstrated by the equation, and

$$D' = \left( \frac{\text{slope}(J_{Ared} \text{ vs. } V^{1/2})}{Kn^{3/2}C} \right)^2$$

revealing that electrochemical processes at both the cathodic and anodic are controlled by the diffusion of the  $I_3^-/I^-$  redox mediator, and there was no interaction except interface electron transfer between the electrode and the electrolyte.<sup>12</sup> As the scan rate increases, the diffusion layer at the electrolyte/CE interface becomes thinner, and the electrochemical polarization at the electrolyte/CE interface increases, therefore resulting in high overpotential and weak reversibility.<sup>13</sup>

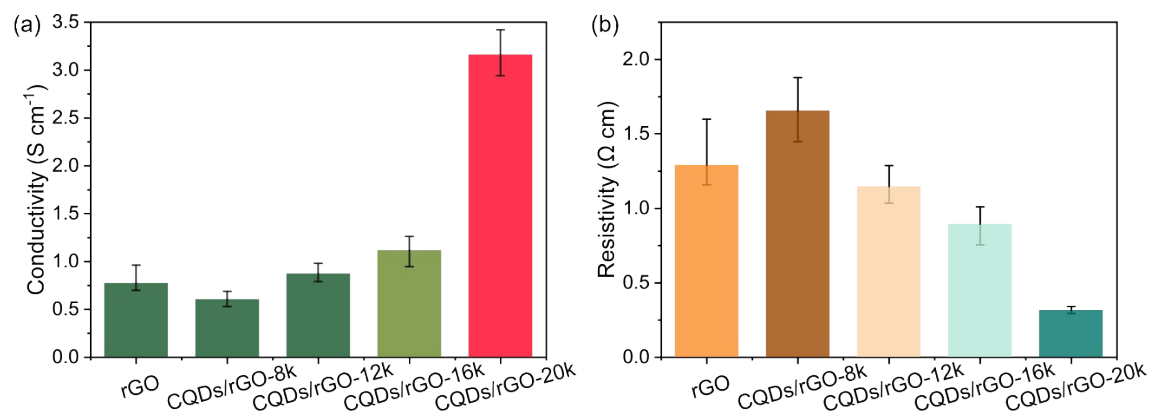


**Fig. S12.** (a) The conductivity and (b) the resistivity of rGO and CQDs/rGO-x tested by four-probe measurements.

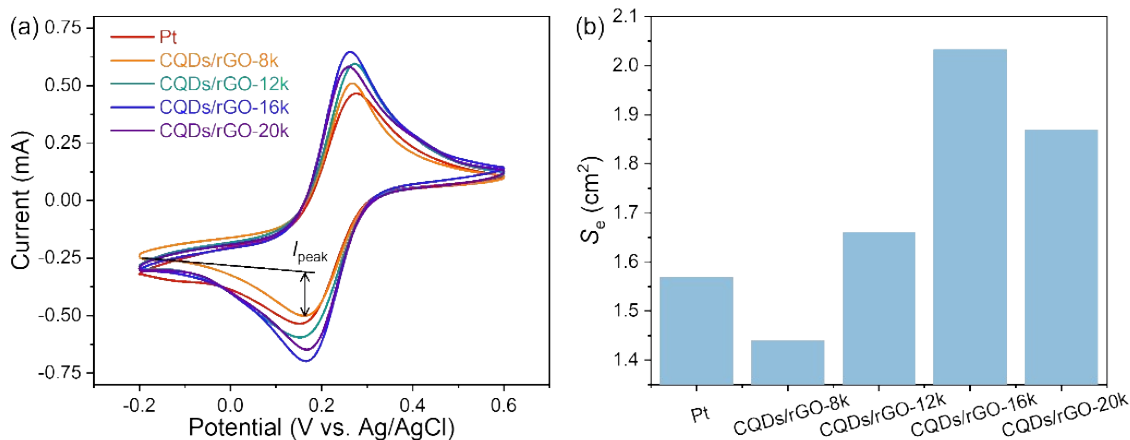


**Fig. S13.** (a) CV curves of the Pt and various CQDs/rGO-x samples measured by using  $[\text{Fe}(\text{CN})_6]^{4-}/[\text{Fe}(\text{CN})_6]^{3-}$  as the redox couple and (b) the corresponding calculated values of  $S_e$ .

The calculation for  $S_e$  is also conducted by the Randles-Sevcik theory:  $I_{\text{peak}} = Kn^{3/2}ACD^{1/2}V^{1/2}$ , where we need to pay attention to some parameters in this case.

Through the deformation formula, we can get:

$$S_e = \frac{I_{\text{peak}}}{2.69 \times 10^5 \times n^{3/2} \times D'^{1/2} \times V^{1/2} \times C}$$

$I_{\text{peak}}$  means the peak currents as shown in **Fig. S13a**.  $n$  means electron transfer number and is equal to 1 here.  $D'$  stands for the diffusion coefficient of the solute, which is  $K_3[\text{Fe}(\text{CN})_6]$  in the aqueous solution here, and equal to  $4.34 \times 10^{-6} \text{ cm}^2 \text{ s}^{-1}$ .  $V$  corresponds to the scan rate and is set to  $10 \text{ mV s}^{-1}$ .  $C$  is electrolyte concentration of  $5 \times 10^{-6} \text{ mol mL}^{-1}$  of  $K_3[\text{Fe}(\text{CN})_6]$ .<sup>14</sup>

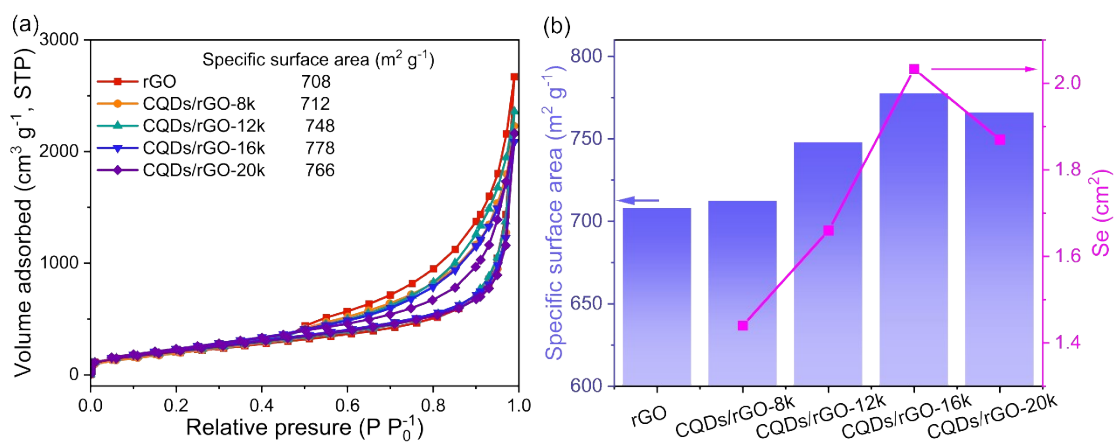


**Fig. S14.** (a)  $N_2$  adsorption/desorption isotherms of rGO and CQDs/rGO-x (inset: the values of the Brunauer-Emmett-Teller (BET) specific surface areas of rGO and CQDs/rGO-x). (b) Specific surface area of the samples and  $S_e$  of the electrode materials.

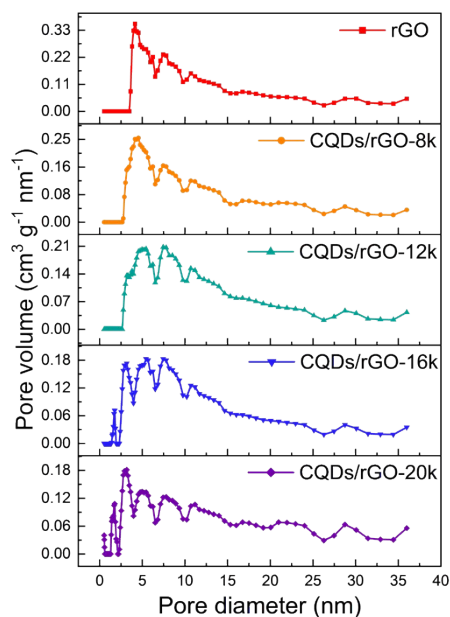


**Fig S15.** The corresponding pore size distributions of the rGO, CQDs/rGO-8k, CQDs/rGO-12k, CQDs/rGO-16k and CQDs/rGO-20k.

The corresponding pore size distributions of the rGO and CQDs/rGO-x were also investigated and exhibited in **Fig. S15**. From the data presented, the rGO and CQDs/rGO-x all feature the mesoporosity-dominated characteristics, while the CQDs/rGO-x have relatively bigger specific surface areas than rGO, and their values gradually increase with the increasing amount of CQDs loading until subsequent decrease for CQDs/rGO-20k. This phenomenon can be attributed to the fact that CPDs play a supporting role between GO layers during the coupling process before carbonization, realized by the assembly of CPDs on the GO surface in the uniformly dispersed solution. Such an effect can inhibit the stacking of GO sheets in the desolventization and carbonization process. In the literatures, the similar effect is also utilized to construct the carbon dots-pillared graphene blocks or graphene quantum dots-induced holey graphene nanosheets to

improve the specific surface area and electrochemical activity.<sup>15, 16</sup> Therefore, the CQDs/rGO-x possess bigger specific surface areas than rGO.

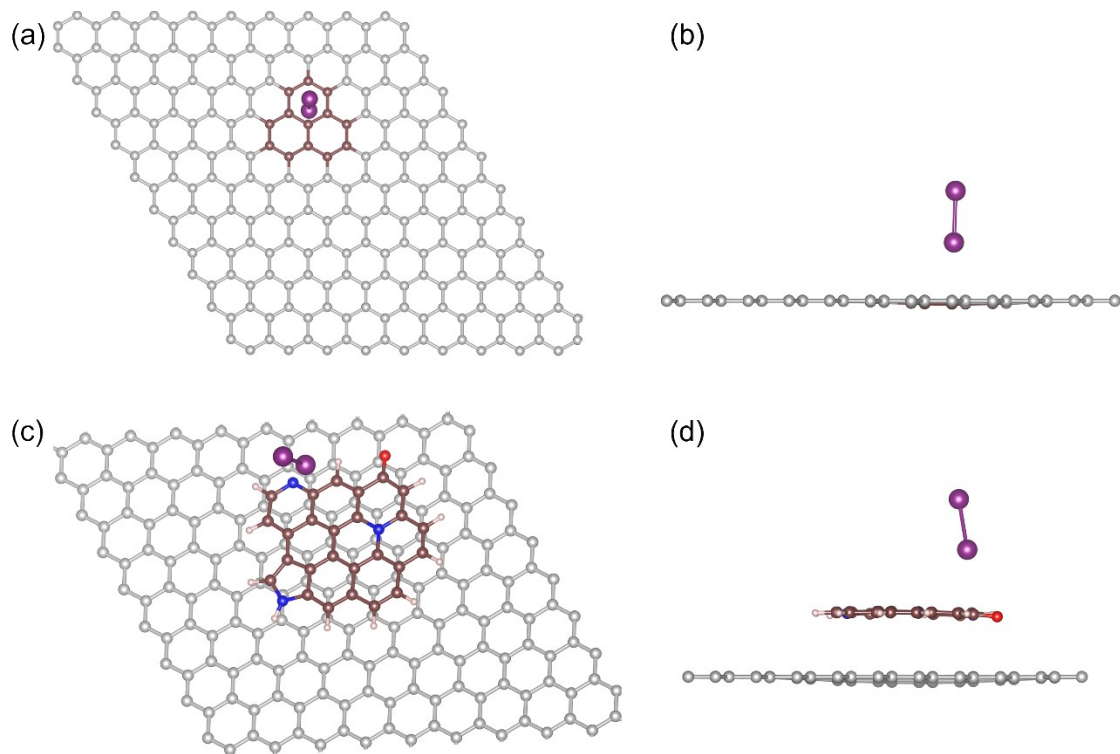


**Fig. S16.** (a) Top view and (b) side view of I<sub>2</sub> adsorption on the basal-plane site of rGO. (c) Top view and (d) side view of I<sub>2</sub> adsorption on the CQDs loading on rGO. Color scheme: C (grey or brown), N (blue), O (red), H (white), and I (purple).

In this work, density functional theory (DFT) calculations are performed with the Vienna ab initio simulation package (VASP).<sup>17, 18</sup> The projector augmented wave (PAW) pseudopotential<sup>19</sup> was adopted to describe the interaction between electrons and ions. The exchange and correlation interactions were described by the generalized gradient approximation (GGA) of Perdew-Burke-Ernzerhof (PBE).<sup>20</sup> The cut-off energy for plane waves was set to 500 eV. The threshold for energy is set at  $10^{-4}$  eV and  $0.05$  eV/Å was for force. The *k*-point mesh was set to  $3 \times 3 \times 1$  for all calculations and the van der Waals

interaction was considered by the empirical correction of the Grimme's scheme (DFT-D3).<sup>21</sup>

It is well known that the overall IRR occurring on the CE can be depicted as a general equation:  $I_3^- (\text{sol}) + 2e^- \leftrightarrow 3I^- (\text{sol})$ , involving a non-electrochemical step (1) and a two-electron transfer electrochemical reaction (2):



where sol means the acetonitrile solution. Reaction (1) reaches equilibrium quickly due to a large rate constant. Therefore, reaction (2) is generally considered to be the rate-determining step of the overall reaction and is mainly investigated in this system. The adsorption of the  $I_2$  molecule on the catalyst surface is the initial and pivotal step in the catalytic reaction. It has been reported that constructing efficient active sites to facilitate the adsorption/dissociation of  $I_2$  molecules for enhancing the rate of reaction (2) is essential to obtain excellent IRR performance.<sup>10</sup> In this work, the adsorption ability of different configurations is evaluated by the adsorption energy ( $E_{\text{ads}}$ ). The  $E_{\text{ads}}$  of the  $I_2$  molecule adsorbed on the surface of the substrates was calculated by the following equation:

$$E_{\text{ads}} = E_{I_2/\text{sub}} - E_{I_2} - E_{\text{sub}}$$

where  $E_{I_2/\text{sub}}$ ,  $E_{I_2}$ , and  $E_{\text{sub}}$  represent the total energy of  $I_2$  molecule adsorbed on the substrates, the energy of  $I_2$  molecule and the energy of substrate system, respectively.

The  $E_{\text{ads}}$  value of the basal-plane site of rGO (**Fig. S16a-b**) is -0.29 eV, while that of the

CQDs loading site on rGO (**Fig. S16c-d**) is  $-0.34$  eV.

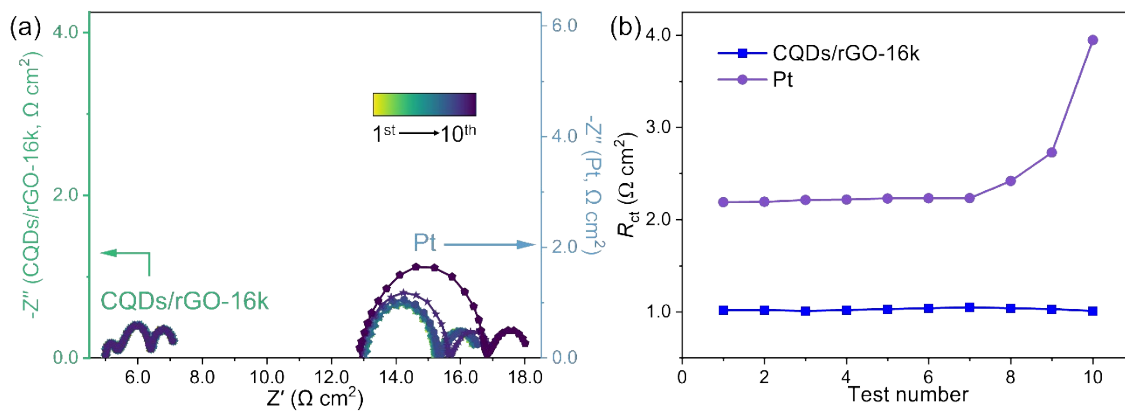


**Fig. S17.** (a) Electrochemical stability and (b) charge transfer resistance ( $R_{ct}$ ) changes versus the EIS test number of the symmetrical dummy cells with Pt or CQDs/rGO-16k CEs, respectively.

**Table S1.** Centrifugal acceleration corresponding to the rotational speed, where the  $g$

represents the gravitational acceleration.

<b>Rotational Speed (rpm)</b>	<b>Centrifugal acceleration (<math>g'</math>, <math>m\ s^{-2}</math>)</b>
8k	7656 <i>g</i>
12k	17227 <i>g</i>
16k	30624 <i>g</i>
20k	47850 <i>g</i>

**Table S2.** Photovoltaic parameters of DSSCs with different CEs.

CE	$V_{oc}$ (V)	FF (%)	$J_{sc}$ (mA cm <sup>-2</sup> )	PCE (%)
Pt	0.73 ± 0.01	69.57 ± 0.86	15.78 ± 0.32	7.97 (+ 0.08, -0.33)
CQDs/rGO-8k	0.71 ± 0.02	67.02 ± 0.44	15.78 ± 0.31	7.50 (+ 0.04, -0.08)
CQDs/rGO-12k	0.72 ± 0.02	70.85 ± 0.49	15.43 ± 0.29	7.89 (+ 0.11, -0.12)
CQDs/rGO-16k	0.74 ± 0.01	71.03 ± 0.25	16.09 ± 0.06	<b>8.36</b> (+ 0.05, -0.08)
CQDs/rGO-20k	0.70 ± 0.02	70.90 ± 0.11	16.60 ± 0.42	8.22 (+ 0.19, -0.08)

**Table S3.** The corresponding values of  $R_{ct}$  and  $R_s$  extracted from the results of the EIS measurement in **Fig. 5e**.

<b>CE</b>	<b><math>R_{ct}</math> (<math>\Omega \text{ cm}^2</math>)</b>	<b><math>R_s</math> (<math>\Omega \text{ cm}^2</math>)</b>
<b>Pt</b>	$1.28 \pm 0.11$	$10.90 \pm 0.30$
<b>CQDs/rGO-8k</b>	$1.38 \pm 0.04$	$5.20 \pm 0.26$
<b>CQDs/rGO-12k</b>	$1.21 \pm 0.05$	$5.03 \pm 0.25$
<b>CQDs/rGO-16k</b>	$0.75 \pm 0.04$	$4.98 \pm 0.25$
<b>CQDs/rGO-20k</b>	$1.01 \pm 0.08$	$4.35 \pm 0.22$

## References

- 1 L. Li, Y. Li, Y. Ye, R. Guo, A. Wang, G. Zou, H. Hou and X. Ji, *ACS Nano*, 2021, **15**, 6872-6885.
- 2 S. Chen, T. Sun, M. Zheng and Z. Xie, *Adv. Funct. Mater.*, 2020, **30**, 2004680.
- 3 V. Ramanan, S. K. Thiyagarajan, K. Raji, R. Suresh, R. Sekar and P. Ramamurthy, *ACS Sustain. Chem. Eng.*, 2016, **4**, 4724-4731.
- 4 S.-Y. Huang, G.-P. Wu, C.-M. Chen, Y. Yang, S.-C. Zhang and C.-X. Lu, *Carbon*, 2013, **52**, 613-616.
- 5 W. Chen, D. Li, L. Tian, W. Xiang, T. Wang, W. Hu, Y. Hu, S. Chen, J. Chen and Z. Dai, *Green Chem.*, 2018, **20**, 4438-4442.
- 6 P. Zhang, D. Bin, J. S. Wei, X. Q. Niu, X. B. Chen, Y. Y. Xia and H. M. Xiong, *ACS Appl. Mater. Interfaces*, 2019, **11**, 14085-14094.
- 7 F. Rigodanza, M. Burian, F. Arcudi, L. Dordevic, H. Amenitsch and M. Prato, *Nat. Commun.*, 2021, **12**, 2640.
- 8 Z.-H. Sheng, L. Shao, J.-J. Chen, W.-J. Bao, F.-B. Wang and X.-H. Xia, *ACS Nano*, 2011, **5**, 4350-4358.
- 9 Y. Zheng, Y. Jiao, Y. Zhu, L. H. Li, Y. Han, Y. Chen, A. Du, M. Jaroniec and S. Z. Qiao, *Nat. Commun.*, 2014, **5**, 4783.
- 10 J. Chang, C. Yu, X. Song, X. Han, Y. Ding, X. Tan, S. Li, Y. Xie, Z. Zhao and J. Qiu, *Nano Energy*, 2021, **89**, 106332.
- 11 C.-J. Liu, S.-Y. Tai, S.-W. Chou, Y.-C. Yu, K.-D. Chang, S. Wang, F. S.-S. Chien, J.-Y. Lin and T.-W. Lin, *J. Mater. Chem.*, 2012, **22**, 21057.
- 12 Y. Ding, C. Yu, J. Chang, C. Yao, J. Yu, W. Guo and J. Qiu, *Small*, 2020, **16**, e1907164.
- 13 J. Wu, Q. Li, L. Fan, Z. Lan, P. Li, J. Lin and S. Hao, *J. Power Sources*, 2008, **181**, 172-176.
- 14 J. Chang, C. Yu, X. Song, X. Tan, Y. Ding, Z. Zhao and J. Qiu, *Angew. Chem. Int. Ed.*, 2021, **60**, 3587-3595.
- 15 M. Ali, R. Riaz, A. S. Anjum, K. C. Sun, H. Li, S. H. Jeong and M. J. Ko, *Carbon*, 2021, **171**, 493-506.
- 16 Z. Liu, L. Zhang, L. Sheng, Q. Zhou, T. Wei, J. Feng and Z. Fan, *Adv. Energy Mater.*, 2018, **8**, 1802042.
- 17 G. Kresse and J. Furthmüller, *Phys. Rev. B*, 1996, **54**, 11169-11186.
- 18 G. Kresse and J. Furthmüller, *Comp. Mater. Sci.*, 1996, **6**, 15-50.
- 19 P. E. Blöchl, *Phys. Rev. B*, 1994, **50**, 17953-17979.
- 20 J. P. Perdew, K. Burke and M. Ernzerhof, *Phys. Rev. Lett.*, 1996, **77**, 3865-3868.
- 21 S. Grimme, J. Antony, S. Ehrlich and H. Krieg, *J Chem. Phys.*, 2010, **132**, 154104.